

Charge and pair density waves in a spin and valley-polarized system at a Van-Hove singularity

Avigail Gil¹ and Erez Berg¹

¹*Department of Condensed Matter Physics, Weizmann Institute of Science, Rehovot 76100, Israel*

We study a single component (i.e., single valley, spin-polarized) two-dimensional electron gas with C_{3v} symmetry tuned to a Van-Hove (VH) singularity. Generically, there may be either three or six VH points at the Fermi level, related to each other by symmetry. Using a renormalization group analysis, we show that when the effective interactions between electrons at the VH points are positive, the system is stable. In contrast, if the effective interactions are negative, the system develops an instability toward either pair density wave (PDW) or charge density wave (CDW) orders, depending on the anisotropy of the dispersion at the VH points. The PDW may have either a single wavevector or multiple wavevectors. The PDW phase with three coexisting wavevectors can support fractional $\frac{h}{6e}$ vortices. The interplay between the geometry of the Fermi surface and the singularity of the density of states is the key that enables PDW formation.

I. INTRODUCTION

In the vast majority of superconductors, the center of mass momentum of the Cooper pairs is zero. This is a consequence of the fact that, in the presence of time reversal symmetry, even a small zero-momentum superconducting order parameter is sufficient to gap the entire Fermi surface (with the possible exception of nodal points in two spatial dimensions). Superconductors whose Cooper pair condensate carries a non-zero momentum are known as pair density wave (PDW) states [1, 2]. Such exotic states have been predicted to occur when time reversal is broken by a Zeeman field, just before being completely destroyed. In this context, they are known as Fulde-Ferrel-Larkin-Ovchinnikov (FFLO) states [3, 4]. Evidence for PDW states in the absence of explicit time reversal breaking has been reported in certain cuprates [5–8] and other materials [9–13].

Generically, a PDW cannot emerge when the interaction strength is weak. Hence, PDWs are usually challenging to obtain theoretically, since they cannot be studied by perturbative techniques. Moreover, in this regime, the PDW state often competes with other forms of electronic order, such as charge density wave (CDW) states. Nevertheless, PDW order has been found in certain models of interacting electrons [14–26].

It thus came as a surprise when superconductivity was recently discovered in rhombohedral four and five-layer graphene (R4G and R5G) in a regime where the spin and valley symmetries are spontaneously broken in the normal state [27]. The most straightforward interpretation of the experiment suggested that the superconducting state is fully spin and valley polarized. Such a state is most likely a PDW, since only states in a single valley are available for pairing near the Fermi energy. Several theoretical works appeared attempting to explain the emergence of this state,

predicting a PDW state whose wavevector is either commensurate [28–32] or incommensurate [33–35] with the underlying graphene lattice.

In this work, we investigate the types of electronic orders that develop when a fully spin and valley polarized two-dimensional system with C_{3v} symmetry is tuned to the vicinity of a Van-Hove (VH) singularity. We study two generic situations with either three or six distinct VH points at the Fermi energy, related to each other by C_{3v} . At the VH singularity, the density of states diverges logarithmically, allowing us to access the electronic instabilities in the weak coupling limit. Moreover, unlike in previous studies of spinful two-dimensional systems near a VH singularity [24, 36–42], our spinless system exhibits only logarithmic divergences in both the particle-particle and particle-hole bare susceptibilities (in the spinful case, the susceptibility in the particle-particle channel typically diverges as the square of the logarithm of the low-energy cutoff [36–38]). Thus, in the spinless case, the two channels can be treated on equal footing, allowing for a better controlled solution of the problem.

Using a weak-coupling renormalization group (RG) analysis, we find that weak repulsive effective interactions at the VH points are marginally irrelevant, and hence the system is stable even when tuned to the VH singularity. For weak attractive interactions, the dominant instability in the low energy limit is determined by the mass anisotropy at the VH points and, in the case of six VH points, also on the angle between the principal axes between neighboring mirror symmetry related VH points. For small anisotropy, the CDW phase is favored. In contrast, for large anisotropy, the system presents an instability towards PDW order. We discuss possible implications of our results for superconductivity and competing orders in rhombohedral multilayer graphene.

II. THREE VH POINTS

A. The Model

We study a C_{3v} symmetric and spin and valley polarized model with three symmetry-related VH points at the Fermi energy. We are interested in the weak-coupling instabilities that occur in the low energy limit. Since the density of states diverges logarithmically near the three VH points, we can treat a simpler problem that includes patches near these points. This type of behavior is exhibited by tuning the density and the displacement field in systems such as twisted bilayer graphene (TBG) [41], twisted double bilayer graphene (TDBG) [42], rhombohedral trilayer graphene (R3G) [43, 44] and R4G [27]. As an illustration, we show the band structure of R4G in Fig. 1a. As can be seen in the figure, at a certain density that depends on the perpendicular displacement field, there are three symmetry-related VH points at the Fermi energy.

We thus consider a model that includes three patches centered at the three VH points at momenta \vec{q}_α , $\alpha = 1, 2, 3$, with one coupling constant g between two electrons in any two different patches, as shown in Fig. 1b. In this model, there is no momentum-independent intra-patch interaction due to the full spin polarization. There is a single inter-patch interaction parameter, g , as a result of the symmetry of the system. Intra and inter-patch momentum dependent interactions are irrelevant under RG, and will be neglected here. We will consider both signs of the coupling g . In Appendix A, we argue that even if the bare interaction is purely repulsive (e.g., Coulomb interactions), the effective low-energy interaction g may be negative.

The low energy Hamiltonian in the patch approximation in the three VH points model is given by:

$$H_3 = \int d^2x \left[\sum_{\alpha=1}^3 \psi_\alpha^\dagger (\varepsilon_\alpha(\vec{k}) - \mu) \psi_\alpha + g \sum_{\alpha < \beta} \psi_\alpha^\dagger \psi_\beta^\dagger \psi_\beta \psi_\alpha \right], \quad (1)$$

where $\psi_\alpha(\vec{x})$ is the fermionic field for an electron on patch $\alpha = 1, 2, 3$. The low energy dispersion around the VH point labeled by α is described by $\varepsilon_\alpha(\vec{k})$, where $\vec{k} = -i\vec{\nabla}$ and μ is the chemical potential. In our model, we assume the mass at the VH point is anisotropic and is characterized by a mass anisotropy parameter, η . Defining

$$\varepsilon_{\vec{k}}(\eta, \varphi) = -\frac{\sqrt{\eta}}{2m} (\cos(\varphi)k_x - \sin(\varphi)k_y)^2 + \frac{1}{2m\sqrt{\eta}} (\sin(\varphi)k_x + \cos(\varphi)k_y)^2, \quad (2)$$

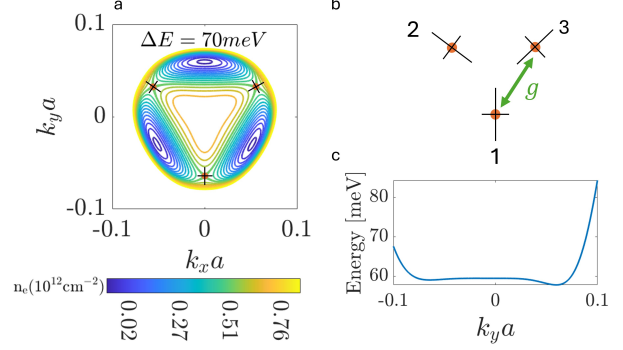


Figure 1: (a) **Iso-energetic lines for R4G** in the +K valley conduction band with a potential difference of $\Delta E = 70\text{meV}$ between the top and bottom layers. The model parameters are taken from [28]. Here, $a \approx 0.246\text{nm}$ is the lattice constant of graphene. The three distinct VH points are drawn schematically in orange on the contours and the black lines represent the principal axes of the saddle points. The VH points are reached for an density of $n_e \approx 0.5 \cdot 10^{12}\text{cm}^{-2}$. (b) **Interactions between electrons near the three VH points.** (c) **Energy cut vs. k_y for $k_x = 0$ of the conduction band of R4G.**

the low energy dispersions near the three VH points at \vec{q}_α , labeled by $\alpha = 1, 2, 3$, are given by

$$\varepsilon_\alpha(\vec{k}) = \varepsilon_{\vec{k}-\vec{q}_\alpha} \left(\eta, \varphi_\alpha = -\frac{2\pi}{3}(\alpha-2) \right). \quad (3)$$

Since the behavior of the system for η is identical to the behavior for $\frac{1}{\eta}$, we restrict our attention to $0 < \eta < 1$. We note that for $\eta = \frac{1}{3}$, we recover the structure of honeycomb tight binding model tuned to the VH singularity [40].

B. RG Analysis

We perform a renormalization group analysis of the Hamiltonian (1) by writing the equivalent action and imposing a cutoff in frequency. I.e. \vec{k} is unbounded, but ω is bounded between $-\Lambda_\omega$ to Λ_ω . In each RG step we integrate out modes with frequency $\Lambda_\omega/s < \omega < \Lambda$ and all momentum, and then rescale the frequency to recover the same cutoff as before. The momenta and frequency scale as:

$$\omega' = s\omega, \quad (4a)$$

$$k' = s^{1/2}k, \quad (4b)$$

$$\psi'(k', \theta, \omega') = s^{-2}\psi(k, \theta, \omega), \quad (4c)$$

where $\vec{k} = k(\cos \theta, \sin \theta)$.

At the tree level, the integration out of the modes and the rescaling of the field leaves the action invariant. To one-loop order, there are three contributions to the renormalization of the coupling constant, known as the BCS diagram, the ZS diagram and the ZS' diagram [45], shown in Fig. 2. We find that the ZS diagram does not contribute to the β function since both of the poles are on the same half plane. The remaining ZS' diagram and BCS diagram each contribute to the flow. The details of the calculation can be found in Appendix B. To one-loop order, the RG flow for the interaction g is given by

$$\dot{g} = -a(\eta)g^2 \equiv -(a_{\text{ZS}'}(\eta) + a_{\text{BCS}}(\eta))g^2 \quad (5)$$

where the flow parameter is $dt = d \log(\Lambda_\omega)$. The full expressions for $a_{\text{ZS}'}(\eta)$ and $a_{\text{BCS}}(\eta)$ are also given in Appendix B.

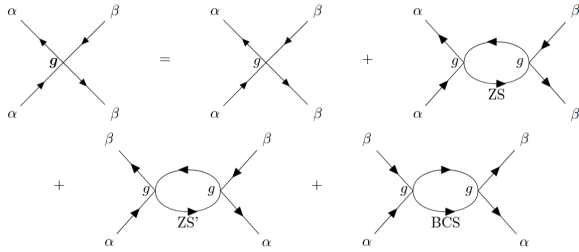


Figure 2: **Diagrams contributing to the renormalization of g** up to one loop order. The indices α and β label the different patches (VH points). The outer frequencies are set to zero, and the frequency inside the loops lies in a shell of width $d\Lambda_\omega$ being integrated over.

For our purpose, the important characteristics of $a(\eta)$ are that it is positive for all η and it diverges at $\eta = \frac{1}{3}$. For $\eta = \frac{1}{3}$, the contribution of the particle-hole channel has a log-squared divergence, due to the perfect nesting of the Fermi surface. Thus, near $\eta = \frac{1}{3}$ our description breaks down. An analysis of the case of $\eta = \frac{1}{3}$ for spinful fermions can be found in [42].

Solving Eq. (5), We find that for an initial repulsive interaction ($g > 0$), g flows towards zero and the system is stable. For an initial attractive interaction, $g < 0$, the interaction diverges under the RG flow. $g(t)$ is given by:

$$g(t) = \frac{1}{a(\eta)(t - t_c)}, \quad (6)$$

where $t_c = \frac{1}{a(\eta)|g(0)|}$, and $E_c = \Lambda_0 \exp(-1/t_c)$ is the critical energy scale where the perturbative treatment breaks down (here, Λ_0 is the initial upper cutoff of the theory).

C. Instabilities

We study the various instabilities the model develops at the energy scale E_c . To probe the tendency to develop each order, we add the various test vertices to the Hamiltonian and track their RG flow.

In the three VH point model, the possible test vertices are

$$\rho_\alpha^{(0)}\psi_\alpha^\dagger\psi_\alpha, \quad \rho_{\alpha,\beta}\psi_\alpha^\dagger\psi_\beta \ (\alpha \neq \beta), \quad \Delta_{\alpha,\beta}\psi_\alpha^\dagger\psi_\beta^\dagger. \quad (7)$$

The diagrams that contribute to their renormalization are shown in Appendix C. The test vertices in Eq. (7) correspond to different types of electronic order: $\rho_\alpha^{(0)}$ is a uniform (zero-wavevector) charge order, $\rho_{\alpha,\beta}$ is a charge density wave between patches α and β with wavevector $\vec{q}_\alpha - \vec{q}_\beta$, and $\Delta_{\alpha,\beta}$ is a pair density wave between α and β whose wavevector is $\vec{q}_\alpha + \vec{q}_\beta$. We find that the test vertices for each instability renormalize with RG in the following way to one loop order:

$$\frac{d\rho_\alpha^{(0)}}{dt} = 0, \quad (8a)$$

$$\frac{d\rho_{\alpha,\beta}}{dt} = -g(t)a_{\text{ZS}'}(\eta)\rho_{\alpha,\beta}, \quad (8b)$$

$$\frac{d\Delta_{\alpha,\beta}}{dt} = -2g(t)a_{\text{BCS}}(\eta)\Delta_{\alpha,\beta}. \quad (8c)$$

From Eqs. (8), we find that uniform charge order is marginal to one loop, while the CDW and PDW orders are suppressed or enhanced depending on the sign of $a_{\text{ZS}'}(\eta)$ and $a_{\text{BCS}}(\eta)$. Solving for the flow

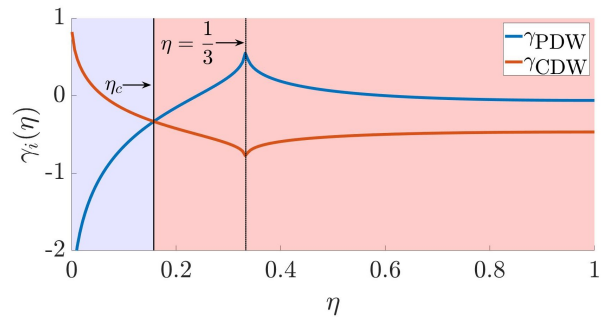


Figure 3: **The exponents of the PDW and CDW susceptibilities**, $\chi_i \approx (t - t_c)^{\gamma_i}$. The inter-patch PDW is shown in blue and the CDW is drawn in orange. For $\eta < \eta_c$, the dominant instability is toward an inter-patch PDW order and for $\eta > \eta_c$ the CDW instability is dominant.

of the vertices, assuming that close to t_c , the order parameter evolves as $(t - t_c)^{\alpha_i}$ ($i = \text{CDW, PDW}$), we

get:

$$\alpha_{\text{CDW}}(\eta) = -\frac{a_{\text{ZS}}(\eta)}{a(\eta)}, \quad (9a)$$

$$\alpha_{\text{PDW}}(\eta) = -2\frac{a_{\text{BCS}}(\eta)}{a(\eta)}. \quad (9b)$$

Near t_c , the susceptibilities diverge as $\chi_i \approx (t - t_c)^{\gamma_i}$ with $\gamma_i = 2\alpha_i + 1$ [46]. The exponents of the susceptibilities $\gamma_i(\eta)$ are plotted in Fig. 3. We find a crossover at $\eta_c \approx 0.157$ where for $\eta < \eta_c$, the instability toward a PDW phase is more dominant.

D. Competition between orders

For $\eta < \eta_c$ ($\eta > \eta_c$) the system can either develop a single q component PDW (CDW) phase or a multiple q component PDW (CDW) phase, respectively. The system will tend toward the state that minimizes the free energy. We treat $\rho_{\alpha,\beta}$ and $\Delta_{\alpha,\beta}$ as order parameters and write the Ginzburg-Landau free energy functional near T_c , up to fourth order in the order parameters,

$$\begin{aligned} F(\Delta_{\alpha,\beta}, \rho_{\alpha,\beta}) = & \frac{1}{2} \sum_{\alpha,\beta} a_{\alpha,\beta}^{\text{P}} (T - T_{\text{P}}) |\Delta_{\alpha,\beta}|^2 + \frac{1}{4} \sum_{\alpha,\beta \neq \gamma,\delta} b_{\alpha,\beta,\gamma,\delta}^{\text{P}} |\Delta_{\alpha,\beta}|^2 |\Delta_{\gamma,\delta}|^2 + \frac{1}{2} \sum_{\alpha,\beta} c_{\alpha,\beta}^{\text{P}} |\Delta_{\alpha,\beta}|^4 + \\ & \frac{1}{4} \sum_{\alpha \neq \beta \neq \gamma} d_{\alpha,\beta,\gamma}^{\text{P}} (\Delta_{\alpha,\beta})^* \Delta_{\gamma,\alpha} \rho_{\beta,\gamma} + c.c. + \frac{1}{4} \sum_{\alpha,\beta \neq \gamma,\delta} u_{\alpha,\beta,\gamma,\delta} |\Delta_{\alpha,\beta}|^2 |\rho_{\gamma,\delta}|^2 + \sum_{\alpha,\beta \neq \gamma,\delta} v_{\alpha,\beta,\gamma,\delta} \Delta_{\alpha,\beta}^* \Delta_{\gamma,\delta} \rho_{\gamma,\alpha}^* \rho_{\beta,\delta} + \\ & \frac{1}{2} \sum_{\alpha,\beta} a_{\alpha,\beta}^{\text{C}} (T - T_{\text{C}}) |\rho_{\alpha,\beta}|^2 + \frac{1}{4} \sum_{\alpha,\beta \neq \gamma,\delta} b_{\alpha,\beta,\gamma,\delta}^{\text{C}} |\rho_{\alpha,\beta}|^2 |\rho_{\gamma,\delta}|^2 + \frac{1}{2} \sum_{\alpha,\beta} c_{\alpha,\beta}^{\text{C}} |\rho_{\alpha,\beta}|^4 + \frac{1}{2} \sum_{\alpha \neq \beta \neq \gamma} d_{\alpha,\beta,\gamma}^{\text{C}} \rho_{\alpha,\beta} \rho_{\gamma,\alpha} \rho_{\beta,\gamma} + c.c. \end{aligned} \quad (10)$$

The calculation of the free energy coefficients $b_{\alpha,\beta,\gamma,\delta}^i$, $c_{\alpha,\beta}^i$, $d_{\alpha,\beta,\gamma}^i$, where $i = \text{P or C}$, and $u_{\alpha,\beta,\gamma,\delta}$, and $v_{\alpha,\beta,\gamma,\delta}$ from the microscopic Hamiltonian is given in Appendix D. We note that $\rho_{\alpha,\beta} = \rho_{\beta,\alpha}^*$ and that $\Delta_{\alpha,\beta} = -\Delta_{\beta,\alpha}$.

We find that, for η near η_c , the Ginzburg-Landau free energy is unbounded from below in the fourth order approximation (see Appendix D). Analyzing the phase diagram thus requires including higher-order terms. We still note, however, that when the system is in a CDW state, it will tend to develop all three components together (which we denote as a $3q$ CDW state). The presence of the cubic term d^{C} in the free energy, dictates that the transition to this state is first order. Since $d^{\text{C}} > 0$, the free energy is minimized when the sum of the three phases is equal to $2\pi(n + \frac{1}{2})$. This constraint leaves two independent phases, that transform under the generators of the two spontaneously broken translation symmetries.

Phenomenologically adding a sixth order term $w [\sum_{\alpha,\beta} (|\Delta_{\alpha,\beta}|^2 + \zeta |\rho_{\alpha,\beta}|^2)]^3$ with $\zeta > 0$ to the expression of the free energy given in Eq. (10) bounds it from below. Minimizing the free energy numerically with respect to the order parameters, we can obtain a qualitative phase diagram (see Fig. 4). We note that all of the phase transitions in this model are first order except the transition from the disordered to $1q$ PDW which is second order.

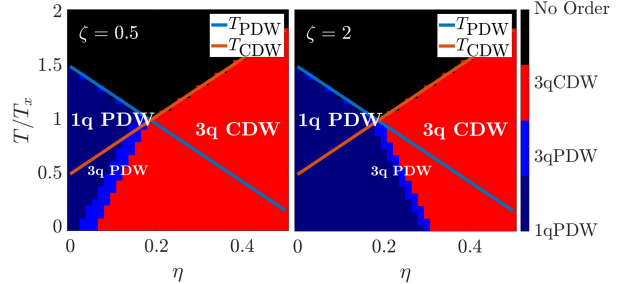


Figure 4: **Qualitative phase diagrams for the three VH point model.** The GL free energy coefficients were set to their values at $\eta = \eta_c$. The coefficient of the phenomenological sixth-order term was set to $w = 0.1$. T_x is the temperature where $T_{\text{PDW}} = T_{\text{CDW}}$ cross at $\eta = \eta_c$. We have assumed the form: $T_{\text{PDW}}(\eta) = T_x [1 - \frac{1}{2\eta_c}(\eta - \eta_c)]$, $T_{\text{CDW}}(\eta) = T_x [1 + \frac{1}{2\eta_c}(\eta - \eta_c)]$. We note that as long as $w > 0$, the phase diagram does not depend on its value. The boundary between the $3q$ CDW phase to the $1q$ PDW phase depends on the value of the phenomenological parameter ζ .

III. SIX VH POINTS

A. Model

We now turn to analyze the second model with six VH points. This structure can arise by tuning the density and the displacement field in systems such as TBG [41], TDBG [42] or R3G [43, 44]. An example of the band structure of R3G with six VH points is plotted in Fig. 5a. The VH points are related to each other either by C_3 rotational symmetry or by mirror symmetry.

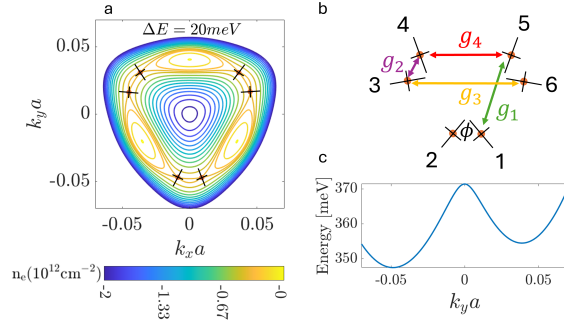


Figure 5: (a) **Iso-energetic lines for R3G vs. \vec{k}** in the +K valley conduction band with a potential difference $\Delta E = 20 \text{ meV}$ between the top and bottom layers. The model parameters were taken from Ref. [44]. The six distinct VH points are drawn schematically in orange on the contours and the black lines represent the principal axes of the saddle points. (b) **Schematics of the distinct inter-patch interactions in a spin polarized model with six VH points.** (c) **Energy cut vs. k_y for $k_x = 0$ of the conduction band of R3G.**

The low energy Hamiltonian in the patch approximation is given by:

$$H_6 = \int d^2x \left[\sum_{\alpha=1}^6 \psi_{\alpha}^{\dagger} (\varepsilon_{\alpha}(\vec{k}) - \mu) \psi_{\alpha} + \sum_{\alpha < \beta} g_{\alpha,\beta} \psi_{\alpha}^{\dagger} \psi_{\beta}^{\dagger} \psi_{\beta} \psi_{\alpha} \right], \quad (11)$$

where $\psi_{\alpha}(\vec{x})$ is the fermionic field for an electron on patch α . The interactions $g_{\alpha,\beta}$ are related to each other through the C_{3v} symmetry of the model:

$$g_{\alpha,\beta} = g_{\beta,\alpha}, \quad (12a)$$

$$g_{1,3} = g_{2,4} = g_{3,5} = g_{4,6} = g_{5,1} = g_{6,2} \equiv g_1, \quad (12b)$$

$$g_{1,2} = g_{3,4} = g_{5,6} \equiv g_2, \quad (12c)$$

$$g_{1,4} = g_{3,6} = g_{5,2} \equiv g_3, \quad (12d)$$

$$g_{2,3} = g_{4,5} = g_{6,1} \equiv g_4. \quad (12e)$$

The low energy dispersion around the VH point labeled by α is described by $\varepsilon_{\alpha}(\vec{k})$ and μ is the chemical

potential. The low energy dispersion around the six VH points is given by

$$\varepsilon_{2\alpha-1}(\vec{k}) = \varepsilon_{\vec{k}-\vec{q}_{\alpha}} \left(\eta, \varphi_{2\alpha-1} = -\frac{2\pi}{3}(\alpha-2) \right), \quad (13a)$$

$$\varepsilon_{2\alpha}(\vec{k}) = \varepsilon_{\vec{k}-\vec{q}_{\alpha}} \left(\eta, \varphi_{2\alpha} = -\frac{2\pi}{3}(\alpha-2) - \phi \right), \quad (13b)$$

where $\varepsilon_{\vec{k}}(\eta, \varphi)$ is given in Eq. (2). Here, we introduced another parameter $0 < \phi < \pi$, which is the angle between the principal axes of patches 1 and 2. (see Fig. 5b). Due to the quadratic approximation of the energy dispersion, the parameter ϕ has a period of π . We note that for $\eta = \frac{1}{3}$ and $\phi = \frac{\pi}{3}$, we recover the structure of the VH points obtained in a tight binding model on a honeycomb lattice.

B. RG Analysis

Just as in the previous model, we turn to RG in order to analyze the stability of the model. The scalings of the fields and momenta are given in Eqs. (4). To tree level, the integration out of the modes and the rescaling of the field leaves the action invariant.

Due to the fact that each interaction involves a momentum transfer of different magnitude, there is no mixing between the different couplings under the RG flow and the RG equations are decoupled. Following a calculation similar to the three VH case, the resulting RG equations can be written as:

$$\dot{g}_{\alpha,\beta} = -A(\eta, \varphi_{\alpha} - \varphi_{\beta}) g_{\alpha,\beta}^2, \quad (14)$$

where the coefficient $A(\eta, \varphi_{\alpha} - \varphi_{\beta})$ depends on the anisotropy of the dispersion and the angle $\varphi_{\alpha} - \varphi_{\beta}$ between the principal axes of the two patches that participate in the coupling $g_{\alpha,\beta}$. As in the three VH case, we can write $A(\eta, \phi)$ as a sum of ZS' and BCS' contributions:

$$A(\eta, \phi) = A^{\text{ZS}'}(\eta, \phi) + A^{\text{BCS}'}(\eta, \phi). \quad (15)$$

The full expressions for $A^{\text{ZS}'}(\eta, \phi)$ and $A^{\text{BCS}'}(\eta, \phi)$ are given in Appendix E.

The flow coefficient $A(\eta, \phi)$ is positive for all η and ϕ , meaning that for initial repulsive interactions ($g_{\alpha,\beta} > 0$), the system remains stable despite the diverging density of states. For initial attractive interactions, all of the interactions diverge under the RG flow for all η and ϕ and the system becomes unstable. We note that, analogously to the three VH case, $A(\eta, \phi = \frac{\pi}{3})$ has a divergence at $\eta = \frac{1}{3}$, due to the presence of a susceptibility that diverges as log squared of the IR cutoff.

C. Instabilities

To probe the tendency to develop each order, we add test vertices to the Hamiltonian and track how they flow. The test vertices and the diagrams that contribute to the renormalization in this model are similar to those in the previous three VH point model and can be found in Appendix C. In this model, we need to consider the following test vertices:

$$\rho_\alpha^{(0)} \psi_\alpha^\dagger \psi_\alpha, \quad \rho_{\alpha,\beta} \psi_\alpha^\dagger \psi_\beta, \quad \Delta_{\alpha,\beta} \psi_\alpha^\dagger \psi_\beta^\dagger. \quad (16)$$

We find that the vertices for each instability renormalize, up to one loop order, in the following way:

$$\frac{d\rho_\alpha^{(0)}}{dt} = 0, \quad (17)$$

$$\frac{d\rho_{\alpha,\beta}}{dt} = -g_{\alpha,\beta}(t) A^{\text{ZS}'}(\eta, \varphi_\alpha - \varphi_\beta) \rho_{\alpha,\beta}, \quad (18)$$

$$\frac{d\Delta_{\alpha,\beta}}{dt} = -2g_{\alpha,\beta}(t) A^{\text{BCS}}(\eta, \varphi_\alpha - \varphi_\beta) \Delta_{\alpha,\beta}. \quad (19)$$

The uniform charge order is marginal to one loop. The CDW and PDW phases are suppressed or enhanced depending on the sign of $A^{\text{ZS}'}(\eta, \varphi_\alpha - \varphi_\beta)$ and $A^{\text{BCS}}(\eta, \varphi_\alpha - \varphi_\beta)$. Solving for the flow of the vertices, assuming that close to the instability, $\Delta_{\alpha,\beta}$ evolves as $(t - t_{c;\alpha,\beta})^{\alpha_{\alpha,\beta}}$, we get:

$$\alpha_{\alpha,\beta}^{\text{PDW}}(\eta, \varphi_\alpha - \varphi_\beta) = -2 \frac{A^{\text{BCS}}(\eta, \varphi_\alpha - \varphi_\beta)}{A(\eta, \varphi_\alpha - \varphi_\beta)} \quad (20)$$

$$\alpha_{\alpha,\beta}^{\text{CDW}}(\eta, \varphi_\alpha - \varphi_\beta) = - \frac{A^{\text{ZS}'}(\eta, \varphi_\alpha - \varphi_\beta)}{A(\eta, \varphi_\alpha - \varphi_\beta)} \quad (21)$$

Near $t_{c;\alpha,\beta}$, the susceptibilities evolve as $\chi_{\alpha,\beta} \approx (t - t_{c;\alpha,\beta})^{\gamma_{\alpha,\beta}}$ with $\gamma_{\alpha,\beta} = 2\alpha_{\alpha,\beta} + 1$.

In Fig. 6, the phase with the most divergent susceptibility is shown as a function of η and ϕ . The various orders correspond to the test vertices from Eqs. (16). As can be seen, the CDW phase dominates most of the phase diagram. The $\text{CDW}_{1,3}$ phase (in which $\langle \psi_1^\dagger \psi_3 \rangle \neq 0$) dominates the area around $\eta = \frac{1}{3}$ where the particle-hole channel no longer has a logarithmic divergence but a log squared divergence on the cutoff.

The rest of the phase diagram can be understood by nesting considerations. For example, the $\text{CDW}_{4,5}$ phase dominates the area between $0 < \phi < \frac{\pi}{3}$ and sufficiently large η . For small anisotropies, at the angle $\phi = \frac{\pi}{6}$ there is a large overlap between the energy dispersions of VH points 4 and 5, 1 and 6, and 2 and 3, which leads to a divergence in the ZS' diagram for g_4 . Hence, the system will tend to develop $\rho_{4,5}, \rho_{1,6}, \rho_{2,3}$ orders. The same happens at the angle $\phi = \frac{\pi}{2}$ for $\rho_{1,2}, \rho_{3,4}, \rho_{5,6}$ orders, etc. The PDW phases are obtained either for large mass anisotropy η , or small angles ϕ around $\frac{n\pi}{3}$ between the two copies of the VH points from the same nesting considerations.

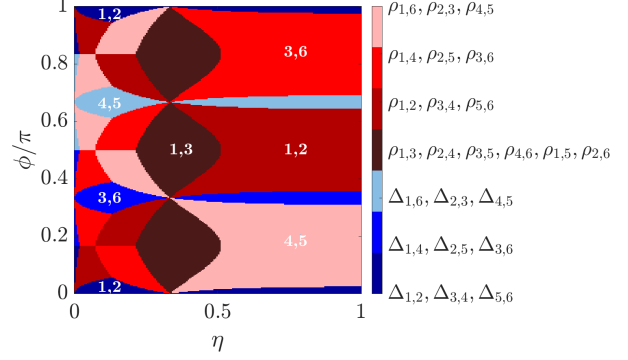


Figure 6: **Leading instability of the six VH point model as a function of η and ϕ .** The type of order with the most divergent susceptibility is indicated for each (η, ϕ) . The various orders correspond to the test vertices given in Eq. (16). The CDW phases dominates most of the phase diagram. PDW phases are realized for large mass anisotropies and for a small range of angles around $\phi = \frac{n\pi}{3}$.

D. Competition between orders

The system can either develop a single q component PDW (CDW) phase, a $3q$ component PDW (CDW) or a $6q$ component CDW. The system will tend toward the state that minimizes the free energy given in Eq. (10). We find, just as in the case of the three VH points model, that the Ginzburg - Landau free energy is unbounded from below up to fourth order. Despite that, we can examine the free energy qualitatively to learn about the various states. The $\text{CDW}_{1,3}$ state has six non-zero CDW components with wavevectors that connect same parity points. This case can be treated, conceptually, as two copies of the three VH points model and therefore developing all $6q$ components minimizes the free energy. Note that this state is generally not periodic but quasi-periodic in space.

The $\text{CDW}_{1,2}$, $\text{CDW}_{3,6}$, $\text{CDW}_{4,5}$, $\text{PDW}_{1,2}$, $\text{PDW}_{3,6}$, and $\text{PDW}_{4,5}$ states each have three components with wavevectors that connect even and odd numbered patches. Within each state, the three components do not share the same patches, resulting in no repulsion between them ($b^C = b^P = 0$). The system will therefore develop all three components to minimize the free energy.

IV. DISCUSSION

A. Summary of results

We have presented two simple models of spin-polarized systems with C_{3v} symmetry, and studied the effects of interactions when the system is tuned to a VH singularity. In these two models, in the weak interaction regime, despite the diverging DOS, the system is stable if the initial interactions are repulsive. When the initial interactions are attractive, both of the systems develop instabilities toward CDW or PDW phases, depending on the anisotropy of the dispersion at the VH point and angle between the principal axes of the dispersions of the two groups of VH points. We note that no other orders (such as nematic order or phase separation) develop in these models, in contrast, e.g., to the Hubbard model on the square lattice near the VH singularity [47]. The model with three VH points develops either a single-q PDW order or 3q CDW order, depending on the anisotropy. close to the transition between these two phases, the system develops a 3q PDW order. The six VH points model can develop various multiple q CDW and PDW orders depending on the mass anisotropy and the angle ϕ between mirror symmetry related VH points.

B. Comparison to other works on PDW at VH points

Previous works studied models for multi-valley C_3 symmetric systems near a VH singularity that develop PDW order [24, 42]. Strictly speaking, in these models, the PDW phase appears at intermediate values of the coupling, where the calculations are not fully under control. This is since the RG flow has to take into account both terms that diverge as the log of the IR cutoff and log-squared divergent terms. In contrast, our model (that starts from a spin and valley polarized state) contains only log divergent singularities, and is thus under better theoretical control. Within this model, PDW order can develop even for asymptotically weak coupling. Note, however, that the fully spin and valley polarized state itself requires a finite interaction strength; here, we have assumed that such a state exists, and studied the effects of residual interactions when a VH singularity is approached.

C. Sign of the initial interaction

Within the patch model, an attractive initial interaction constant between the VH points is required

to obtain either the CDW or the PDW phase. This leaves the question how such an attractive interaction may arise microscopically when the bare Coulombic interactions are repulsive. In this case, the renormalization that may lead to a change in sign in the effective inter-patch interaction has to come from degrees of freedom that are not too close to the Fermi energy.

Conceptually, we may treat the problem in a two-step RG procedure: starting from the full electronic dispersion, we first integrate out degrees of freedom down to a small but finite energy cutoff, and then use the patch RG to renormalize the interaction further. Unfortunately, we do not know of a fully controlled way to carry out the first step of this procedure. As a crude approximation, we may use the random phase approximation (RPA) to describe the effective inter-patch interaction that serves as the initial condition for the patch RG. As we show in Appendix A, this indeed gives $g_1 < 0$ for realistic parameters for tetralayer graphene.

D. Experimental signatures

As mentioned earlier, evidence for superconductivity in spin and valley polarized states was recently found in R4G and R5G [27]. Moreover, a superconducting diode effect was detected in magic angle twisted trilayer graphene with zero external magnetic field, indicating possible valley polarization in the superconducting state [48]. Of course, in these materials, the interaction strength is expected to be strong, so it is not clear to what extent the weak-coupling analysis presented here is applicable. Nevertheless, the weak-coupling analysis may capture some of the qualitative physics. We conclude this section by pointing out different possible experimental signatures of different PDW states found in this work.

The 3q PDW state breaks translational symmetry spontaneously, and is accompanied by a 3q CDW order (this follows from the d^P term in the free energy, see Eq. (10)). Interestingly, this state supports fractional $\frac{h}{6e}$ quantum vortices bound to lattice dislocations [49, 50]. For completeness, we present a derivation of this result in Appendix F. If the fractional vortices are the most stable, this state can thus be detected by magnetic scanning superconducting quantum interference device (SQUID) measurements, by comparing the number of vortices to the applied magnetic field. Even in the absence of an external magnetic field, disorder is expected to nucleate lattice dislocations that bind $\frac{h}{6e}$ fractional vortices.

The 1q PDW state does not break translational symmetry (since it is invariant under a combination

of translation and a gauge transformation, implying that any gauge-invariant observable is also translationally invariant). Thus, in this phase, the charge density has the period of the underlying graphene lattice. However, this phase breaks C_3 symmetry spontaneously due to the choice of the wavevector of the PDW, implying that the critical current is anisotropic.

Finally, we note that in the weak-coupling limit treated in this work, the PDW and CDW states are expected to have gapless fermionic excitations. In particular, the PDW states have Bogoliubov Fermi surfaces [14, 51, 52]. This is since the PDW order only gaps out states near the VH points. At intermediate to strong coupling strengths, the entire Fermi surface may become gapped.

ACKNOWLEDGMENTS

We thank Noga Bashan, Vladimir Calvera, Andrey Chubukov, Steve Kivelson, Pavel Nosov, Oskar Vafek, and Yaar Vituri for useful discussions. This work was supported by the European Research Council (ERC) under grant HQMAT (Grant Agreement No. 817799), by the Simons Foundation Collaboration on New Frontiers in Superconductivity (Grant SFI-MPS-NFS-00006741-03), and NSF-BSF Award No. DMR-2310312. We thank the hospitality of the Kavli Institute for Theoretical Physics, supported in part by grant NSF PHY-2309135.

Appendix A: Initial value of the interaction within RPA

Here, we calculate the initial value of the interaction, $g(0)$, that enters the patch RG calculation for realistic parameters for R4G, within the random phase approximation (RPA). We demonstrate that even though the bare interaction is repulsive, $g(0)$ can be negative, leading to instabilities towards CDW or PDW states.

Our procedure can be thought of as a two-step RG process. The bare interaction is taken to be a dual-gate screened Coulomb potential, $V_{0,q} = \frac{e^2}{2\epsilon q} \tanh(qd)$, where d is the distance to the gates and ϵ is the effective dielectric constant of the surrounding insulator. Integrating out high energy modes down to a small but finite cutoff Λ_0 , we obtained a renormalized interaction, screened by high-energy modes. This renormalized interaction is then projected to the VH patches, obtaining $g(0)$. As a crude approximation, we use RPA to compute the effective interaction in the first step of the renormalization. This is justified since the original interaction is long-ranged (assuming that d is larger than the inter-electron spacing in the R4G), and hence $V_{0,q}$ is strongly peaked at $q = 0$.

The RPA screened interaction is given by [53]:

$$V_{RPA}(\vec{q}) = \frac{V_{0,q}}{1 + \Pi_{0,\vec{q}} V_{0,q}}, \quad (\text{A1})$$

where $\Pi_{0,\vec{q}} = \frac{1}{A} \sum_{\vec{k}} |\Lambda_{\vec{k},\vec{q}}|^2 \frac{f(\epsilon_{\vec{k}}) - f(\epsilon_{\vec{k}+\vec{q}})}{\epsilon_{\vec{k}+\vec{q}} - \epsilon_{\vec{k}}}$ is the static polarization function. $\epsilon_{\vec{k}}$ is the energy of the electron, $f(x)$ is the Fermi-Dirac distribution and $\Lambda_{\vec{k},\vec{q}} = \langle u_{\vec{k}} | u_{\vec{k}+\vec{q}} \rangle$ is the overlap matrix element between states of the electron band at momenta \vec{k} and $\vec{k} + \vec{q}$. We implement a low-energy cutoff by performing the calculation at a non-zero temperature T .

For the band structure of R4G, we use the model given in [28], with a displacement field corresponding to a potential difference $\Delta E = 70\text{meV}$ between the top and bottom layers. The calculations were performed for the +K valley doped to the VH density at a temperature of $T = 100\text{mK}$, $\epsilon = 5\epsilon_0$ and $d = 40\text{nm}$. We chose \vec{q} as a vector pointing between VH points 2 and 3 (see Fig. 1) with a varying magnitude q where $q = q_{\text{VH}}$ is the magnitude of vector connecting VH points 2 and 3. Plotted in Fig. 7 are the static polarization function, the gate-screened Coulomb potential and the effective RPA potential. We find that the initial interaction constant in the three VH point model $g_1(0) = V_{\text{RPA}}(0) - V_{\text{RPA}}(q_{\text{VH}}) |\langle u_{\vec{q}_2} | u_{\vec{q}_3} \rangle|^2 < 0$ (for the R4G band structure, we find that $|\langle u_{\vec{q}_2} | u_{\vec{q}_3} \rangle|^2 \approx 0.5$), resulting in initial attractive interactions between the VH patches. We note that there is no divergence in the polarization at $q = 0$ and at $q = q_{\text{VH}}$ due to the finite temperature.

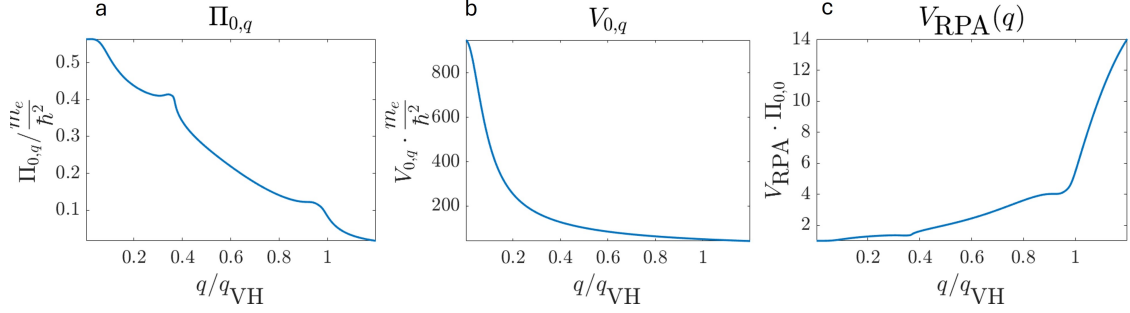


Figure 7: **The effective interaction potential for R4G using RPA** (a) The static polarization calculated along the vector connecting VH points 2 and 3 (see Fig. 1) at a temperature $T = 100\text{mK}$. (b) The screened Coulomb potential where we used $\varepsilon = 5\varepsilon_0$ and $d = 40\text{nm}$. (c) The effective RPA interaction potential.

Appendix B: Three VH points RG of the interaction

In this section, we will present the calculations for the RG flow equation in the three VH points model. The expressions for the flow coefficients defined in Eq. (5) are given by

$$a_{\text{ZS}}(\eta) = -\frac{2m\sqrt{\eta}}{\sqrt{3}\pi(1+\eta)} \log\left(\frac{\sqrt{3}\eta + 4\sqrt{\eta} + \sqrt{3}}{\sqrt{3}\eta - 4\sqrt{\eta} + \sqrt{3}}\right), \quad (\text{B1})$$

$$a_{\text{BCS}}(\eta) = -\frac{4m\sqrt{\eta}}{\pi\sqrt{(\eta-3)(3\eta-1)}} \arctan\left(\frac{\sqrt{3}\eta - 4\sqrt{\eta} + \sqrt{3}}{\sqrt{(\eta-3)(3\eta-1)}}\right), \quad (\text{B2})$$

where the flow parameter is $dt = d\log(\Lambda_\omega)$. The diagrams that contribute to the beta function up to one loop order are shown in Fig. 2. The contribution of the ZS diagram is given by:

$$\delta^{\text{ZS}}g = g^2 \iint_{d\Lambda} d\omega d\vec{k} \frac{1}{i\omega - \varepsilon_1(\vec{k})} \frac{1}{i\omega - \varepsilon_1(\vec{k})}, \quad (\text{B3})$$

where ω is the loop frequency and $\varepsilon_i(\vec{k})$ is the low energy dispersion at VH point labeled i . The full expression for the energy dispersion is given in Eq. (3). This diagram does not contribute to the flow because both of the poles are on the same half of the plane, meaning we can always choose a contour that does not enclose them. The ZS' contribution is given by:

$$\delta^{\text{ZS}'}g = g^2 \iint_{d\Lambda} d\omega d\vec{k} \frac{1}{i\omega - \varepsilon_1(\vec{k})} \frac{1}{i\omega - \varepsilon_3(\vec{k})}. \quad (\text{B4})$$

As discussed in Chapter II B, due to the complexity of the energy dispersion in momentum, we will renormalize the frequency:

$$\delta^{\text{ZS}'}g = g^2 \int_{d\Lambda_\omega} d\omega \int d\vec{k} \frac{1}{i\omega - \varepsilon_1(\vec{k})} \frac{1}{i\omega - \varepsilon_3(\vec{k})}. \quad (\text{B5})$$

Transforming to polar coordinates, we denote:

$$\varepsilon_i(\vec{k}) = \frac{k^2}{2m\sqrt{\eta}} f_i(\theta), \quad (\text{B6})$$

where $f_i(\theta) = \sin^2\left(\theta + \frac{2\pi(i-2)}{3}\right) - \eta \cos^2\left(\theta + \frac{2\pi(i-2)}{3}\right)$. Inserting this into Eq. (B5):

$$\begin{aligned} \delta^{\text{ZS}'} g &= g^2 \int_{d\Lambda_\omega} \frac{d\omega}{2\pi} \int_0^{\Lambda_k} \frac{k dk}{2\pi} \int_0^{2\pi} \frac{d\theta}{2\pi} \frac{1}{i\omega - \frac{k^2}{2m\sqrt{\eta}} f_1(\theta)} \frac{1}{i\omega - \frac{k^2}{2m\sqrt{\eta}} f_3(\theta)} = \\ &= \frac{2m\sqrt{\eta} g^2}{2(2\pi)^3} \int_{d\Lambda_\omega} \frac{d\omega}{\omega} \int_0^{2\pi} d\theta \frac{\arctan\left(\frac{\Lambda_k^2}{2m\sqrt{\eta}\omega} f_3(\theta)\right) - \arctan\left(\frac{\Lambda_k^2}{2m\sqrt{\eta}\omega} f_1(\theta)\right)}{f_1(\theta) - f_3(\theta)} + \frac{i}{2} \frac{\log\left(\frac{\left(\frac{\Lambda_k^2}{2m\sqrt{\eta}} f_1(\theta)\right)^2 + \omega^2}{\left(\frac{\Lambda_k^2}{2m\sqrt{\eta}} f_3(\theta)\right)^2 + \omega^2}\right)}{f_1(\theta) - f_3(\theta)}. \end{aligned} \quad (\text{B7})$$

The renormalization is taken over positive and negative frequency shells eliminating the complex part of the integral. Taking the momentum cutoff to infinity, we receive:

$$\delta^{\text{ZS}'} g = -\frac{2m\sqrt{\eta}}{16\pi^2} \int_0^{2\pi} d\theta \frac{\text{sign}(f_3(\theta)) - \text{sign}(f_1(\theta))}{f_3(\theta) - f_1(\theta)} \frac{d\Lambda_\omega}{\omega} g^2. \quad (\text{B8})$$

We find that the integral depends on the sign of the angular part of the dispersion. In the case of the ZS' diagram, the integral vanishes when the angular part of the both of the energy dispersion functions have the same sign. Performing the integral on opposite sign regions, we receive the result mentioned in Eq. (B1).

Moving to the final diagram, the contribution of the BCS diagram is given by:

$$\delta^{\text{BCS}} g = -\frac{1}{2} g^2 \iint_{d\Lambda} d\omega d\vec{k} \frac{1}{i\omega - \varepsilon_1(\vec{k})} \frac{1}{-i\omega - \varepsilon_3(\vec{k})}. \quad (\text{B9})$$

Performing the calculation the same manner, we find that the BCS integral depends on the sign of the angular part of the energy dispersions. Unlike the previous case, this integral vanishes when they have opposite signs.

$$\delta^{\text{BCS}} g = -\frac{2m\sqrt{\eta}}{32\pi^2} \int_0^{2\pi} d\theta \frac{\text{sign}(f_3(\theta)) + \text{sign}(f_1(\theta))}{f_1(\theta) + f_3(\theta)} \frac{d\Lambda_\omega}{\omega} g^2. \quad (\text{B10})$$

Performing the integral on equal sign regions, we receive the result mentioned in Eq. (B2).

Appendix C: Three VH points RG of the test vertices

The diagrams that contribute to the RG of the test vertices are given in Fig. 8.

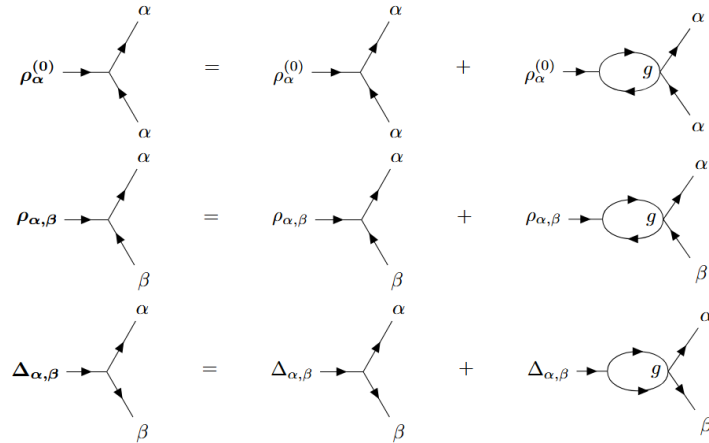


Figure 8: The diagrams that contribute to the renormalization of the various test vertices up to one loop order. The labels on the diagrams are the labels of the VH point. The loop frequency lies in a shell of width $d\Lambda_\omega$ being integrated over.

Appendix D: Three VH points Ginzburg Landau

In this part, we will present the calculations of the Ginzburg-Landau free energy coefficients b_i , c_i , d_i , $u_{\alpha\beta,\gamma\delta}$, and $v_{\alpha\beta,\gamma\delta}$ in the three VH points model, in order to determine the leading phase under T_c . The contributing diagrams that we will calculate can be seen in Fig. 10. The expression for b_P is given by:

$$b_P(\eta) = \int_{-\infty}^{\infty} \frac{d\omega}{2\pi} \int_{-\infty}^{\infty} \frac{d^2k}{(2\pi)^2} \frac{1}{i\omega - \varepsilon_1(\vec{k})} \frac{1}{i\omega - \varepsilon_1(\vec{k})} \frac{1}{-i\omega - \varepsilon_2(\vec{k})} \frac{1}{-i\omega - \varepsilon_3(\vec{k})}, \quad (D1)$$

where ω is the loop frequency and $\varepsilon_i(\vec{k})$ is the low energy dispersion at the VH point labeled i . The full expression for the energy dispersion is given in Eq. (3).

Following a similar calculation to the one shown in Appendix B, we transform to polar coordinates, and change the variable $k^2 = 2m\sqrt{\eta}|\omega|x$:

$$b_P(\eta) = \frac{m\sqrt{\eta}}{(2\pi)^3} \int_{-\infty}^{\infty} \frac{d\omega}{|\omega|^3} \int_0^{2\pi} d\theta \int_0^{\infty} dx \frac{1}{i\text{sgn}(\omega) - xf_1(\theta)} \frac{1}{i\text{sgn}(\omega) - xf_1(\theta)} \frac{1}{-i\text{sgn}(\omega) - xf_2(\theta)} \frac{1}{-i\text{sgn}(\omega) - xf_3(\theta)}. \quad (D2)$$

Integrating over positive and negative frequencies gives the real part of the integral:

$$b_P(\eta) = \frac{m\sqrt{\eta}}{(2\pi)^3} \int_{\lambda_\omega}^{\infty} \frac{d\omega}{\omega^3} \int_0^{2\pi} d\theta \int_0^{\infty} dx \, 2\text{Re} \left(\frac{1}{i - xf_1(\theta)} \frac{1}{i - xf_1(\theta)} \frac{1}{i + xf_2(\theta)} \frac{1}{i + xf_3(\theta)} \right), \quad (D3)$$

where we added a lower frequency cutoff λ_ω . The lower cutoff λ_ω is equivalent to a finite temperature calculation. Performing the integral over ω and the integral over x from 0 to $\Lambda_x \rightarrow \infty$, we receive:

$$b_P(\eta) = \frac{m\sqrt{\eta}}{16\pi^2\lambda_\omega^2} \int_0^{2\pi} d\theta \left(\frac{f_1(f_1f_2 + f_1f_3 + 2f_2f_3)\text{sgn}(f_1)}{(f_1 + f_2)^2(f_1 + f_3)^2} + \frac{f_2^2\text{sgn}(f_2)}{(f_1 + f_2)^2(f_2 - f_3)} + \frac{f_3^2\text{sgn}(f_3)}{(f_1 + f_3)^2(f_3 - f_2)} \right). \quad (D4)$$

The remaining angular part of this integral was calculated numerically.

The remaining Ginzburg-Landau free energy coefficients can be calculated in a similar way. These coefficients are given by:

$$c_P(\eta) = \frac{1}{2} \int \frac{d\omega}{2\pi} \int \frac{d^2k}{(2\pi)^2} \frac{1}{i\omega - \varepsilon_1(\vec{k})} \frac{1}{i\omega - \varepsilon_1(\vec{k})} \frac{1}{-i\omega - \varepsilon_3(\vec{k})} \frac{1}{-i\omega - \varepsilon_3(\vec{k})}, \quad (D5a)$$

$$d_P(\eta) = - \int \frac{d\omega}{2\pi} \int \frac{d^2k}{(2\pi)^2} \frac{1}{i\omega - \varepsilon_1(\vec{k})} \frac{1}{i\omega - \varepsilon_2(\vec{k})} \frac{1}{-i\omega - \varepsilon_3(\vec{k})}, \quad (D5b)$$

$$b_C(\eta) = \int \frac{d\omega}{2\pi} \int \frac{d^2k}{(2\pi)^2} \frac{1}{i\omega - \varepsilon_1(\vec{k})} \frac{1}{i\omega - \varepsilon_1(\vec{k})} \frac{1}{i\omega - \varepsilon_2(\vec{k})} \frac{1}{i\omega - \varepsilon_3(\vec{k})}, \quad (D5c)$$

$$c_C(\eta) = \frac{1}{2} \int \frac{d\omega}{2\pi} \int \frac{d^2k}{(2\pi)^2} \frac{1}{i\omega - \varepsilon_1(\vec{k})} \frac{1}{i\omega - \varepsilon_1(\vec{k})} \frac{1}{i\omega - \varepsilon_3(\vec{k})} \frac{1}{i\omega - \varepsilon_3(\vec{k})}, \quad (D5d)$$

$$d_C(\eta) = - \int \frac{d\omega}{2\pi} \int \frac{d^2k}{(2\pi)^2} \frac{1}{i\omega - \varepsilon_1(\vec{k})} \frac{1}{i\omega - \varepsilon_2(\vec{k})} \frac{1}{i\omega - \varepsilon_3(\vec{k})}, \quad (D5e)$$

$$u_{2323}(\eta) = - \int \frac{d\omega}{2\pi} \int \frac{d^2k}{(2\pi)^2} \frac{1}{-i\omega - \varepsilon_3(\vec{k})} \frac{1}{-i\omega - \varepsilon_2(\vec{k})} \frac{1}{i\omega - \varepsilon_3(\vec{k})} \frac{1}{i\omega - \varepsilon_2(\vec{k})}, \quad (D5f)$$

$$u_{2312}(\eta) = - \int \frac{d\omega}{2\pi} \int \frac{d^2k}{(2\pi)^2} \frac{1}{-i\omega - \varepsilon_3(\vec{k})} \frac{1}{i\omega - \varepsilon_2(\vec{k})} \frac{1}{i\omega - \varepsilon_1(\vec{k})} \frac{1}{i\omega - \varepsilon_2(\vec{k})}. \quad (D5g)$$

where $u_{\alpha\beta,\alpha\beta}$ are all equal to each other, $u_{\alpha\beta\neq\gamma\delta}$ are all equal to each other and $v_{\alpha\beta,\gamma\delta} = 0$ due to the Gaussian averaging that cancels out.

Following the same steps as above: transforming to polar coordinates and integrating over ω and the

magnitude of \vec{k} , we obtain:

$$c_P(\eta) = \frac{m\sqrt{\eta}}{16\pi^2\lambda_\omega^2} \int_0^{2\pi} d\theta \left(\frac{f_1 f_3 \text{sgn}(f_1)}{(f_1 + f_3)^3} + \frac{f_1 f_3 \text{sgn}(f_3)}{(f_1 + f_3)^3} \right), \quad (\text{D6a})$$

$$d_P(\eta) = -\frac{m\sqrt{\eta}}{4\pi^3\lambda_\omega} \int_0^{2\pi} d\theta \left(\frac{f_1 f_2 \log\left(\frac{f_1}{f_2}\right) + f_1 f_3 \log\left(\frac{f_1}{f_3}\right) + f_3 f_2 \log\left(\frac{f_3}{f_2}\right)}{(f_1 - f_2)(f_1 + f_3)(f_2 + f_3)} \right), \quad (\text{D6b})$$

$$b_C(\eta) = \frac{m\sqrt{\eta}}{16\pi^2\lambda_\omega^2} \int_0^{2\pi} d\theta \left(-\frac{f_1(f_1 f_2 + f_1 f_3 - 2f_2 f_3) \text{sgn}(f_1)}{(f_1 - f_2)^2(f_1 - f_3)^2} + \frac{f_2^2 \text{sgn}(f_2)}{(f_1 - f_2)^2(f_2 - f_3)} + \frac{f_3^2 \text{sgn}(f_3)}{(f_1 - f_3)^2(f_3 - f_2)} \right), \quad (\text{D6c})$$

$$c_C(\eta) = \frac{m\sqrt{\eta}}{16\pi^2\lambda_\omega^2} \int_0^{2\pi} d\theta \left(-\frac{f_1 f_3 \text{sgn}(f_1)}{(f_1 - f_3)^3} + \frac{f_1 f_3 \text{sgn}(f_3)}{(f_1 - f_3)^3} \right), \quad (\text{D6d})$$

$$d_C(\eta) = -\frac{m\sqrt{\eta}}{4\pi^3\lambda_\omega} \int_0^{2\pi} d\theta \left(\frac{f_1 f_2 \log\left(\frac{f_2}{f_1}\right) + f_1 f_3 \log\left(\frac{f_1}{f_3}\right) + f_3 f_2 \log\left(\frac{f_3}{f_2}\right)}{(f_1 - f_2)(f_1 - f_3)(f_2 - f_3)} \right), \quad (\text{D6e})$$

$$u_{2323}(\eta) = -\frac{m\sqrt{\eta}}{16\pi^2\lambda_\omega^2} \int_0^{2\pi} d\theta \left(\frac{f_2 \text{sgn}(f_2)}{f_2^2 - f_3^2} - \frac{f_3 \text{sgn}(f_3)}{f_2^2 - f_3^2} \right), \quad (\text{D6f})$$

$$u_{2312}(\eta) = \frac{m\sqrt{\eta}}{16\pi^2\lambda_\omega^2} \int_0^{2\pi} d\theta \left(\frac{f_1^2 \text{sgn}(f_1)}{(f_1 - f_2)^2(f_1 + f_3)} + \frac{f_2(f_2 f_3 - f_1 f_2 - 2f_2 f_3) \text{sgn}(f_2)}{(f_1 - f_2)^2(f_2 + f_3)^2} + \frac{f_3^2 \text{sgn}(f_3)}{(f_1 + f_3)(f_2 + f_3)^2} \right). \quad (\text{D6g})$$

The remaining angular part of these integrals was calculated numerically. The value of these coefficients as a function of η is plotted in Fig. 9.

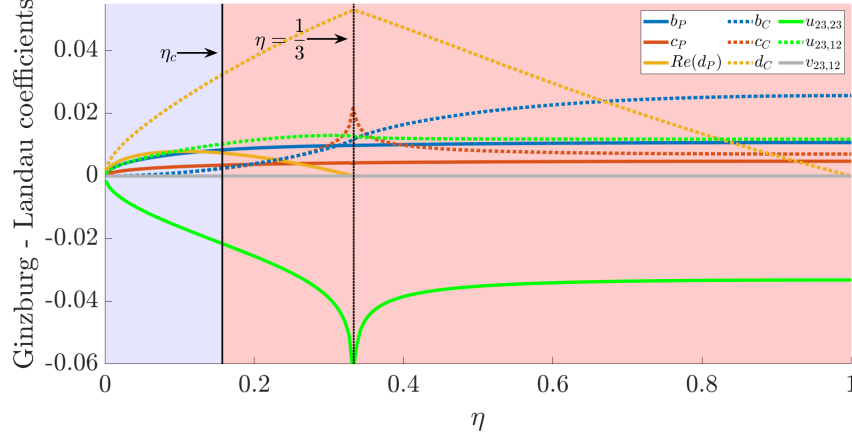


Figure 9: The Ginzburg - Landau coefficients as a function of η calculated from the diagrams given in Fig. 10.

To prove that the Ginzburg-Landau free energy is not bounded from below, we define:

$$F_4 = \begin{pmatrix} |\Delta_{12}|^2 \\ |\Delta_{23}|^2 \\ |\Delta_{31}|^2 \\ |\rho_{12}|^2 \\ |\rho_{23}|^2 \\ |\rho_{31}|^2 \end{pmatrix}^T \begin{pmatrix} c_P & b_P & b_P & u_{1212} & u_{1223} & u_{1231} \\ b_P & c_P & b_P & u_{2312} & u_{2323} & u_{2331} \\ b_P & b_P & c_P & u_{3112} & u_{3123} & u_{3131} \\ c_P & b_P & b_P & u_{1212} & u_{2311} & u_{3112} \\ b_P & c_P & b_P & u_{1223} & u_{2323} & u_{3123} \\ b_P & b_P & c_P & u_{1231} & u_{2331} & u_{3131} \end{pmatrix}_\eta \begin{pmatrix} |\Delta_{12}|^2 \\ |\Delta_{23}|^2 \\ |\Delta_{31}|^2 \\ |\rho_{12}|^2 \\ |\rho_{23}|^2 \\ |\rho_{31}|^2 \end{pmatrix}. \quad (\text{D7})$$

By looking at the eigenvalues and eigenvectors of the matrix in Eq. (D7) we can determine whether the quartic term in the Ginzburg - Landau free energy is unbounded from below. If there exists a negative

eigenvalue, and the corresponding eigenvector has non-negative entries, the free energy is unbounded in the direction of the corresponding eigenvector. If the corresponding eigenvector includes negative entries, we need to examine its projection on each of the surfaces of the non-negative region and check whether the corresponding minor matrix has negative eigenvalues on that surface.

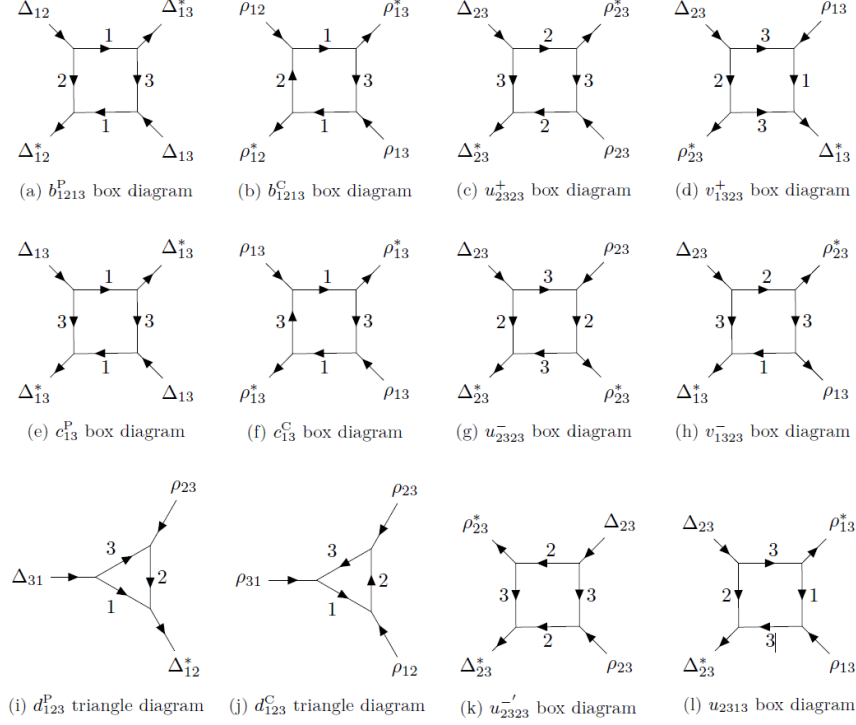


Figure 10: Examples of the contributing diagrams to the Ginzburg-Landau free energy in the three VH points model.

Appendix E: Six VH points RG of the interaction

We follow the same procedure as in Appendix B, to calculate the RG flow of the interaction g_2 . The expressions for the flow coefficients $A^{\text{ZS}'}(\eta, \phi)$ and $A^{\text{BCS}}(\eta, \phi)$, defined in Eqs. (15), for $\phi < \frac{\pi}{2}$, are given by:

$$A^{\text{ZS}'}(\eta, \phi) = \frac{m\sqrt{\eta}}{2\pi^2(\eta+1)\sin(\phi)} \log \left(\frac{\tan \left(\arcsin \left(\sqrt{\frac{\eta}{\eta+1}} + \frac{\phi}{2} \right) \right)}{\tan \left(\arcsin \left(\sqrt{\frac{\eta}{\eta+1}} - \frac{\phi}{2} \right) \right)} \right), \quad (\text{E1})$$

$$A_2^{\text{BCS}}(\eta, \phi) = \frac{m\sqrt{\eta}}{\pi^2(\eta+1)\alpha_{\text{BCS}}} \operatorname{arctanh} \left(\frac{\left(\frac{\eta-3}{\eta+1} - \cos(2\phi) \right) \tan \left(\arcsin \left(\sqrt{\frac{\eta}{\eta+1}} \right) - \phi \right) - \sin(2\phi)}{\alpha_{\text{BCS}}} \right) \\ + \frac{m\sqrt{\eta}}{\pi^2(\eta+1)\alpha_{\text{BCS}}} \operatorname{arctanh} \left(\frac{\left(\frac{\eta-3}{\eta+1} - \cos(2\phi) \right) \sqrt{\eta} + \sin(2\phi)}{\alpha_{\text{BCS}}} \right), \quad (\text{E2})$$

where $\alpha_{\text{BCS}} = \sqrt{2 \left(\cos(2\phi) - 2 \left(\frac{2\eta}{\eta+1} \right)^2 + \frac{8\eta}{\eta+1} - 1 \right)}$.

Appendix F: Fractional vortices in 3q PDW states

An analysis of the fundamental defects of a three-component PDW appeared in Ref. [49]. We provide a simple derivation of the existence of $\frac{h}{6e}$ vortices for completeness.

The PDW order parameter can be written in real space as

$$\Delta(\vec{x}) = |\Delta| \sum_{i=1}^3 e^{i\vec{Q}_i \cdot \vec{x} + i\varphi_i}, \quad (\text{F1})$$

where the three PDW components have the same magnitude, $|\Delta|$, by C_{3v} symmetry. The wavevectors $\vec{Q}_{1,2,3}$ are given in Fig. 11, and are related to the wavevectors of the VH locations, $\vec{q}_{1,2,3}$, by: $\vec{Q}_1 = \vec{q}_2 + \vec{q}_3$, $\vec{Q}_2 = \vec{q}_1 + \vec{q}_3$, $\vec{Q}_3 = \vec{q}_1 + \vec{q}_2$. Table I lists how the phase fields φ_i transform under the symmetries of the system.

Table I: Transformation properties of the phase fields under symmetry operations.

Charge $U(1)$	Translation by \vec{a}	C_3
$\varphi_i \rightarrow \varphi_i + 2\alpha$, $\vec{A} \rightarrow \vec{A} - \frac{h}{e} \nabla \alpha$.	$\varphi_i \rightarrow \varphi_i + \vec{Q}_i \cdot \vec{a}$	$\varphi_1 \rightarrow \varphi_2$ $\varphi_2 \rightarrow \varphi_3$ $\varphi_3 \rightarrow \varphi_1$

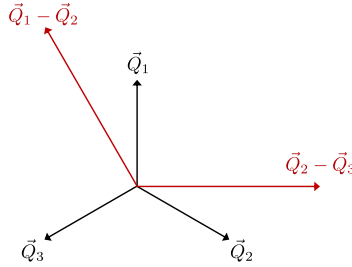


Figure 11: The vectors $\vec{Q}_{1,2,3}$ of the three components of the PDW. The two vectors $\vec{Q}_1 - \vec{Q}_2$ and $\vec{Q}_2 - \vec{Q}_3$ are reciprocal lattice vectors of the lattice corresponding to the modulation of the charge in the PDW state.

In order to write the free energy, it is convenient to change variables to

$$\begin{aligned} \phi_0 &= \varphi_1 + \varphi_2 + \varphi_3, \\ \phi_1 &= \varphi_1 - \frac{1}{2}(\varphi_2 + \varphi_3), \\ \phi_2 &= \varphi_2 - \varphi_3. \end{aligned} \quad (\text{F2})$$

Here, ϕ_0 is the phase of the condensate which transforms under a charge $U(1)$ transformation, and $\phi_{1,2}$ are proportional to the two components of the displacement vector $\vec{u} = (u_1, u_2)$ along two orthogonal directions. Note that ϕ_0 is translationally invariant, whereas $\phi_{1,2}$ are charge neutral, i.e., they do not transform under charge $U(1)$. In terms of these variables, the free energy can be written as

$$F = \int d^2x \frac{1}{2} \kappa_P \left(\vec{\nabla} \phi_0 + \frac{6e}{h} \vec{A} \right)^2 + F_{el}[\phi_1, \phi_2]. \quad (\text{F3})$$

Here, κ_P is the phase stiffness, and F_{el} is the elastic energy of the PDW:

$$F_{el}[\phi_1, \phi_2] = \int d^2x \left(\frac{\kappa_0}{2} [\partial_1 \phi_1 + \partial_2 \phi_2]^2 + \frac{\kappa_1}{2} [(\partial_1 \phi_1 - \partial_2 \phi_2)^2 + (\partial_1 \phi_2 + \partial_2 \phi_1)^2] \right), \quad (\text{F4})$$

where κ_0 and κ_1 are elastic constants related to the bulk and shear moduli of the PDW crystal. The spatial derivatives $\partial_{1,2}$ are taken in the direction of the displacements corresponding to $\phi_{1,2}$.

Requiring that the order parameter is single-valued, the three phases have to satisfy

$$\oint \vec{\nabla} \varphi_1 \cdot d\vec{x} = 2\pi n_i \quad (\text{F5})$$

with integer n_i for any closed curve. Consider an elementary point defect around which $(n_1, n_2, n_3) = (1, 0, 0)$. Using Eq. (F2), we find that for a curve around such a defect,

$$\begin{aligned} \oint \vec{\nabla} \phi_0 \cdot d\vec{x} &= 2\pi, \\ \oint \vec{\nabla} \phi_1 \cdot d\vec{x} &= 2\pi, \\ \oint \vec{\nabla} \phi_2 \cdot d\vec{x} &= 0. \end{aligned} \quad (\text{F6})$$

From (F3), we see that this corresponds to a flux $\Phi = \oint \vec{A} \cdot d\vec{x} = -\frac{\hbar}{6e} \oint \vec{\nabla} \phi_0 \cdot d\vec{x} = -\frac{\hbar}{6e}$. Therefore, this defect corresponds to a flux $|\Phi| = \frac{\hbar}{6e}$ bound to an elementary lattice dislocation with Burgers vector $(a_c, 0)$, where a_c is the triangular lattice corresponding to the charge modulation in the PDW state (or, equivalently, to the periodicity of $|\Delta(\vec{x})|^2$).

-
- [1] Erez Berg, Eduardo Fradkin, and Steven A. Kivelson, “Theory of the striped superconductor,” *Phys. Rev. B* **79**, 064515 (2009).
 - [2] Daniel F Agterberg, JC Séamus Davis, Stephen D Edkins, Eduardo Fradkin, Dale J Van Harlingen, Steven A Kivelson, Patrick A Lee, Leo Radzihovsky, John M Tranquada, and Yuxuan Wang, “The physics of pair-density waves: Cuprate superconductors and beyond,” *Annual Review of Condensed Matter Physics* **11**, 231–270 (2020).
 - [3] Peter Fulde and Richard A. Ferrell, “Superconductivity in a Strong Spin-Exchange Field,” *Phys. Rev.* **135**, A550–A563 (1964).
 - [4] A. I. Larkin and Yu N. Ovchinnikov, “Nonuniform state of superconductors,” *Zh. Eksp. Teor. Fiz* **47**, 1136 (1964).
 - [5] Q. Li, M. Hücker, G. D. Gu, A. M. Tsvelik, and J. M. Tranquada, “Two-Dimensional Superconducting Fluctuations in Stripe-Ordered $\text{La}_{1.875}\text{Ba}_{0.125}\text{CuO}_4$,” *Phys. Rev. Lett.* **99**, 067001 (2007).
 - [6] E. Berg, E. Fradkin, E.-A. Kim, S. A. Kivelson, V. Oganesyan, J. M. Tranquada, and S. C. Zhang, “Dynamical Layer Decoupling in a Stripe-Ordered High- T_c Superconductor,” *Phys. Rev. Lett.* **99**, 127003 (2007).
 - [7] J. M. Tranquada, G. D. Gu, M. Hücker, Q. Jie, H.-J. Kang, R. Klingeler, Q. Li, N. Tristan, J. S. Wen, G. Y. Xu, Z. J. Xu, J. Zhou, and M. v. Zimmermann, “Evidence for unusual superconducting correlations coexisting with stripe order in $\text{La}_{1.875}\text{Ba}_{0.125}\text{CuO}_4$,” *Phys. Rev. B* **78**, 174529 (2008).
 - [8] Stephen D Edkins, Andrey Kostin, Kazuhiro Fujita, Andrew P Mackenzie, Hiroshi Eisaki, S Uchida, Subir Sachdev, Michael J Lawler, E-A Kim, JC Séamus Davis, *et al.*, “Magnetic field-induced pair density wave state in the cuprate vortex halo,” *Science* **364**, 976–980 (2019).
 - [9] Hong Li, Dongjin Oh, Mingu Kang, He Zhao, Brenden R. Ortiz, Yuzki Oey, Shiang Fang, Zheng Ren, Chris Jozwiak, Aaron Bostwick, Eli Rotenberg, Joseph G. Checkelsky, Ziqiang Wang, Stephen D. Wilson, Riccardo Comin, and Ilija Zeljkovic, “Small Fermi Pockets Intertwined with Charge Stripes and Pair Density Wave Order in a Kagome Superconductor,” *Phys. Rev. X* **13**, 031030 (2023).
 - [10] Yanzhao Liu, Tianheng Wei, Guanyang He, Yi Zhang, Ziqiang Wang, and Jian Wang, “Pair density wave state in a monolayer high-T_c iron-based superconductor,” *Nature* **618**, 934–939 (2023).
 - [11] Qiangqiang Gu, Joseph P Carroll, Shuqiu Wang, Sheng Ran, Christopher Broyles, Hasan Siddiquee, Nicholas P Butch, Shanta R Saha, Johnpierre Paglione, JC Séamus Davis, *et al.*, “Detection of a pair density wave state in UTe_2 ,” *Nature* **618**, 921–927 (2023).
 - [12] Anuva Aishwarya, Julian May-Mann, Arjun Raghavan, Laimei Nie, Marisa Romanelli, Sheng Ran, Shanta R Saha, Johnpierre Paglione, Nicholas P Butch, Eduardo Fradkin, *et al.*, “Magnetic-field-sensitive charge density waves in the superconductor UTe_2 ,” *Nature* **618**, 928–933 (2023).
 - [13] A Devarakonda, A Chen, S Fang, D Graf, M Kriener, AJ Akey, DC Bell, T Suzuki, and JG Checkelsky, “Evidence of striped electronic phases in a structurally modulated superlattice,” *Nature* **631**, 526–530 (2024).
 - [14] Erez Berg, Eduardo Fradkin, Steven A Kivelson, and John M Tranquada, “Striped superconductors: how spin, charge and superconducting orders intertwine in the cuprates,” *New Journal of Physics* **11**, 115004 (2009).
 - [15] Erez Berg, Eduardo Fradkin, and Steven A. Kivelson, “Pair-Density-Wave Correlations in the Kondo-Heisenberg Model,” *Phys. Rev. Lett.* **105**, 146403 (2010).

- (2010).
- [16] Yuxuan Wang, Daniel F. Agterberg, and Andrey Chubukov, “Coexistence of Charge-Density-Wave and Pair-Density-Wave Orders in Underdoped Cuprates,” *Phys. Rev. Lett.* **114**, 197001 (2015).
 - [17] Oskar Vafek, James M. Murray, and Vladimir Cvetkovic, “Superconductivity on the Brink of Spin-Charge Order in a Doped Honeycomb Bilayer,” *Phys. Rev. Lett.* **112**, 147002 (2014).
 - [18] Jordan Venderley and Eun-Ah Kim, “Evidence of pair-density wave in spin-valley locked systems,” *Science advances* **5**, eaat4698 (2019).
 - [19] Cheng Peng, Yi-Fan Jiang, Thomas P Devereaux, and Hong-Chen Jiang, “Precursor of pair-density wave in doping Kitaev spin liquid on the honeycomb lattice,” *npj Quantum Materials* **6**, 64 (2021).
 - [20] Zhaoyu Han and Steven A. Kivelson, “Pair density wave and reentrant superconducting tendencies originating from valley polarization,” *Phys. Rev. B* **105**, L100509 (2022).
 - [21] Ya-Hui Zhang and Ashvin Vishwanath, “Pair-density-wave superconductor from doping Haldane chain and rung-singlet ladder,” *Phys. Rev. B* **106**, 045103 (2022).
 - [22] Kevin S Huang, Zhaoyu Han, Steven A Kivelson, and Hong Yao, “Pair-density-wave in the strong coupling limit of the Holstein-Hubbard model,” *npj Quantum Materials* **7**, 17 (2022).
 - [23] Daniel Shaffer, F. J. Burnell, and Rafael M. Fernandes, “Weak-coupling theory of pair density wave instabilities in transition metal dichalcogenides,” *Phys. Rev. B* **107**, 224516 (2023).
 - [24] Yi-Ming Wu, Zhengzhi Wu, and Hong Yao, “Pair-Density-Wave and Chiral Superconductivity in Twisted Bilayer Transition Metal Dichalcogenides,” *Phys. Rev. Lett.* **130**, 126001 (2023).
 - [25] Yi-Fan Jiang and Hong Yao, “Pair-Density-Wave Superconductivity: A Microscopic Model on the 2D Honeycomb Lattice,” *Phys. Rev. Lett.* **133**, 176501 (2024).
 - [26] Zhengzhi Wu, Yi-Ming Wu, and Fengcheng Wu, “Pair density wave and loop current promoted by Van Hove singularities in moiré systems,” *Phys. Rev. B* **107**, 045122 (2023).
 - [27] Tonghang Han, Zhengguang Lu, Yuxuan Yao, Lihan Shi, Jixiang Yang, Junseok Seo, Shenyong Ye, Zhenghan Wu, Muyang Zhou, Haoyang Liu, *et al.*, “Signatures of chiral superconductivity in rhombohedral graphene,” *arXiv preprint arXiv:2408.15233* (2024).
 - [28] Yang-Zhi Chou, Jihang Zhu, and Sankar Das Sarma, “Intravalley spin-polarized superconductivity in rhombohedral tetralayer graphene,” (2024), *arXiv:2409.06701 [cond-mat.supr-con]*.
 - [29] Max Geier, Margarita Davydova, and Liang Fu, “Chiral and topological superconductivity in isospin polarized multilayer graphene,” (2024), *arXiv:2409.13829 [cond-mat.supr-con]*.
 - [30] Guillermo Parra-Martinez, Alejandro Jimeno-Pozo, Vo Tien Phong, Hector Sainz-Cruz, Daniel Kaplan, Peleg Emanuel, Yuval Oreg, Pierre A. Pantaleon, Jose Angel Silva-Guillen, and Francisco Guinea, “Band Renormalization, Quarter Metals, and Chiral Superconductivity in Rhombohedral Tetralayer Graphene,” (2025), *arXiv:2502.19474 [cond-mat.str-el]*.
 - [31] Minh Kim, Abigail Timmel, Long Ju, and Xiao-Gang Wen, “Topological chiral superconductivity beyond pairing in a Fermi liquid,” *Phys. Rev. B* **111**, 014508 (2025).
 - [32] Gal Shavit and Jason Alicea, “Quantum Geometric Unconventional Superconductivity,” (2024), *arXiv:2411.05071 [cond-mat.supr-con]*.
 - [33] Hui Yang and Ya-Hui Zhang, “Topological incommensurate Fulde-Ferrell-Larkin-Ovchinnikov superconductor and Bogoliubov Fermi surface in rhombohedral tetra-layer graphene,” (2024), *arXiv:2411.02503 [cond-mat.supr-con]*.
 - [34] Yinqi Chen and Constantin Schrade, “Intrinsic superconducting diode effect and nonreciprocal superconductivity in rhombohedral graphene multilayers,” (2025), *arXiv:2503.16391 [cond-mat.supr-con]*.
 - [35] Filippo Gaglioli, Daniele Guerici, and Liang Fu, “Spontaneous vortex-antivortex lattice and Majorana fermions in rhombohedral graphene,” (2025), *arXiv:2503.16384 [cond-mat.supr-con]*.
 - [36] I. Dzyaloshinskii, “Superconducting transitions due to van hove singularities in the electron spectrum,” *Sov. Phys. JETP* **66**, 848 (1987).
 - [37] H. J. Schulz, “Superconductivity and Antiferromagnetism in the Two-Dimensional Hubbard Model: Scaling Theory,” *Europhysics Letters* **4**, 609 (1987).
 - [38] D. Poilblanc P. Lederer, G. Montambaux, “Antiferromagnetism and superconductivity in a quasi two-dimensional electron gas. Scaling theory of a generic Hubbard model,” *J. Phys. France* **48** (1987).
 - [39] Nobuo Furukawa, T. M. Rice, and Manfred Salmhofer, “Truncation of a Two-Dimensional Fermi Surface due to Quasiparticle Gap Formation at the Saddle Points,” *Phys. Rev. Lett.* **81**, 3195–3198 (1998).
 - [40] Rahul Nandkishore, Leonid S Levitov, and Andrey V Chubukov, “Chiral superconductivity from repulsive interactions in doped graphene,” *Nature Physics* **8**, 158–163 (2012).
 - [41] Yuri Sherkunov and Joseph J. Betouras, “Electronic phases in twisted bilayer graphene at magic angles as a result of Van Hove singularities and interactions,” *Phys. Rev. B* **98**, 205151 (2018).
 - [42] Yi-Ting Hsu, Fengcheng Wu, and S. Das Sarma, “Topological superconductivity, ferromagnetism, and valley-polarized phases in moiré systems: Renormalization group analysis for twisted double bilayer graphene,” *Phys. Rev. B* **102**, 085103 (2020).
 - [43] Haoxin Zhou, Tian Xie, Areg Ghazaryan, Tobias Holder, James R. Ehrets, Eric M. Spanton, Takashi Taniguchi, Kenji Watanabe, Erez Berg, Maksym Serbyn, and Andrea F. Young, “Half- and quarter-metals in rhombohedral trilayer graphene,” *Nature* **598**, 429–433 (2021).
 - [44] S. Chatterjee, T. Wang, E. Berg, and M. Zaletel, “Inter-valley coherent order and isospin fluctuation

- mediated superconductivity in rhombohedral trilayer graphene,” *Nature Communications* **13**, 6013 (2022).
- [45] R. Shankar, “Renormalization-group approach to interacting fermions,” *Rev. Mod. Phys.* **66**, 129–192 (1994).
 - [46] Yu-Ping Lin and Rahul M. Nandkishore, “Chiral twist on the high- T_c phase diagram in moiré heterostructures,” *Phys. Rev. B* **100**, 085136 (2019).
 - [47] Christoph J. Halboth and Walter Metzner, “ d -Wave Superconductivity and Pomeranchuk Instability in the Two-Dimensional Hubbard Model,” *Phys. Rev. Lett.* **85**, 5162–5165 (2000).
 - [48] Jiang-Xiazi et al. Lin, “Zero-field superconducting diode effect in small-twist-angle trilayer graphene,” *Nature Physics* **18**, 1221–1227 (2022).
 - [49] D. F. Agterberg, M. Geracie, and H. Tsunetsugu, “Conventional and charge-six superfluids from melting hexagonal Fulde-Ferrell-Larkin-Ovchinnikov phases in two dimensions,” *Phys. Rev. B* **84**, 014513 (2011).
 - [50] Sen Zhou and Ziqiang Wang, “Chern Fermi pocket, topological pair density wave, and charge-4e and charge-6e superconductivity in kagomé superconductors,” *Nature Communications* **13**, 7288 (2022).
 - [51] Shirit Baruch and Dror Orgad, “Spectral signatures of modulated d -wave superconducting phases,” *Phys. Rev. B* **77**, 174502 (2008).
 - [52] P. M. R. Brydon, D. F. Agterberg, Henri Menke, and C. Timm, “Bogoliubov Fermi surfaces: General theory, magnetic order, and topology,” *Phys. Rev. B* **98**, 224509 (2018).
 - [53] Areg Ghazaryan, Tobias Holder, Erez Berg, and Maksym Serbyn, “Multilayer graphenes as a platform for interaction-driven physics and topological superconductivity,” *Phys. Rev. B* **107**, 104502 (2023).